Conserved Variable Analysis of the Convective Boundary Layer Thermodynamic Structure over the Tropical Oceans

ALAN K. BETTS*
West Pawlet, VT 05775

BRUCE A. ALBRECHT
Department of Meteorology, Pennsylvania State University, University Park, PA 16802

(Manuscript received 2 April 1986, in final form 30 July 1986)

ABSTRACT

An analysis of FGGE dropwindsonde data using conserved thermodynamic variables shows mixing line structures for the convective boundary layer over the equatorial Pacific. Deeper boundary layers show a double structure. Reversals of the gradients of mixing ratio and equivalent potential temperature above the boundary-layer top are present in all the averages and suggest that the origin of the air sinking into the boundary layer needs further study.

1. Introduction

The convective boundary layer (CBL) over the oceans plays an essential role in regulating the transport of energy and moisture upward into the atmosphere from the surface. Since the global climate depends on these transports, increasing attention is being given to the parameterization of the CBL in global forecast models (Betts and Miller, 1986; Betts, 1986; Albrecht et al., 1986). Recently, Betts (1985) suggested that diagnostic studies of the CBL could be used to guide the development of a mixing line boundary layer cloud parameterization that has proved useful in global models (Betts, 1986; Betts and Miller, 1986). The approach suggested by Betts (1985) is based on conserved variable methods. In this paper we use such an analysis to study the convective boundary layer over the central equatorial Pacific.

Conserved variable analyses have a long history. Rossby (1932) suggested the use of characteristic diagrams of potential and equivalent potential temperatures (θ, θ_E) to analyze air mass structure. Riehl (1954, 1979) made extensive use of (θ_E, p) plots to study the vertical structure of the tropical atmosphere. More recently, Paluch (1979) introduced plots of wet equivalent potential temperature and total water (θ_q, q_T) to study vertical mixing in nonprecipitating clouds, and Deardorff (1980) used liquid water potential temperature and total water (θ_L, q_T) to analyze mixing in stratocumulus. Betts (1982) showed that these conserved variable diagrams could be summarized as a saturation point (SP) diagram since the conserved variables (θ_L, θ_E, q_T) are functions of temperature and pressure (T^*, p^*) at the air-parcel saturation level. Betts (1985) suggested that the vertical gradient of SP through a CBL could be used to characterize the vertical thermodynamic mixing. In a typical CBL (Betts, 1982, 1983, 1984) we find a gradient of SP that is close to the mixing line formed by the thermodynamic mixing of air near the surface with air from the free atmosphere above the CBL (which is usually being incorporated into the CBL through a stable capping layer).

A number of previous studies have been made of the oceanic convective boundary layer. Riehl et al. (1951) and Neiburger et al. (1961) analyzed the inversion structure over the northeastern Pacific. There have been several experiments to study boundary layer structure in the Atlantic: the Meteor expedition (Ficker, 1936), the Atlantic Tradewind Experiment (ATEX) (Augstein et al., 1973, 1974), the Barbados Oceanographic and Meteorological Experiment (BOMEX) (Holland and Rasmusson, 1973) and the GARP Atlantic Tropical Experiment (GATE) (see reviews by Augstein, 1978; Augstein and Hinzpeter, 1982; Houze and Betts, 1981). The First GARP Global Experiment (FGGE) provided an opportunity to analyze boundary layer structure over the equatorial Pacific using an extensive dropwindsonde dataset that was collected during 1979 (Julian, 1982). A conventional analysis of the vertical structure for disturbed and undisturbed conditions during January and February of 1979 (mean soundings and cross sections) was made by Firestone and Albrecht (1986). Here we shall present a more detailed conserved variable analysis of a subset of this data to study the thermodynamic structure through

* Visiting Scientist: NASA Goddard Space Flight Center.

and above the CBL. Then we shall make some comparisons with the structure obtained by similar analyses of ATEX and BOMEX datasets.

2. Data processing and methodology

a. Datasets

The primary dataset comes from dropwindsonde data collected during the First Special Observing Period (SOP-1) of FGGE (Julian, 1982). Although the main purpose of these observations was to obtain winds over the tropical oceans, they also provided high vertical resolution ($\approx$4 mb) thermodynamic data. In this study we use data collected from flights between Hawaii and the equator between 15 January and 20 February 1979. Figure 1 shows the approximate flight paths and the grouping by geographical locations that was used for analysis. In this paper we shall analyze a subset of the soundings from regions I and IV just north of the equator between 165°W–175°E and 130°–145°W. These datasets contain those soundings that had a low-level inversion. Soundings were included in this inversion class if the moist adiabat through θ_E at 980 mb (representing the temperature path of an ascending nonentraining air parcel) showed positive buoyancy above the lifting condensation level (LCL) of the 980 mb air, but again intersected the θ_{ES} sounding below 600 mb. These soundings typically have a low-level inversion between 720 and 870 mb. Figure 3 is an average rather than an individual sounding, but the vertical line through θ_E at 980 mb, which shows positive buoyancy between 950 and 850 mb, illustrates this selection process.

The temperature and dewpoint data were analyzed between 600 and 1000 mb. They were first smoothed in the vertical using a 1–2–1 filter and then interpolated to 10 mb levels. Potential temperature, θ; mixing ratio, q; virtual potential temperature, θ_v; equivalent potential temperature θ_E; saturation equivalent potential temperature, θ_{ES}; temperature and pressure at the saturation level (SL, here the LCL), T^*, p^*; and a variable

$$\mathcal{P} = p^* - p$$

(the difference between air parcel pressure and saturation level pressure) were calculated from temperatures and dewpoints. We shall find $\mathcal{P}$ to be a useful variable to distinguish between layers that are in and above the CBL. In the absence of radiation and mixing processes, the saturation level p^* of a parcel is unchanged by vertical (dry or moist adiabatic) motion, so that if air above the CBL subsides faster than the radiative increase of p^*, then $\mathcal{P}$ can reach relatively large negative values (see section 4f). A few soundings were rejected that had unrealistic vertical gradients of θ.

The ATEX dataset used in this study was for the undisturbed period 7–12 February 1969 from the ship *Planet* and is discussed in Augstein et al. (1973). The BOMEX dataset used here is a three-day average for undisturbed convective conditions (22–24 June 1969), which was kindly supplied by E. Rasmusson.

b. Averaging procedure and data quality

We shall present only averages of the data (except for the scatterplot in Fig. 7). Several averaging methods were investigated, but it was found that averaging the T, θ and q fields at each 10 mb pressure level best preserved the vertical thermodynamic profiles of the individual soundings. Individual values that differed by more than two standard deviations from the mean were eliminated. The saturation-level variables (T^*, p^*) for the average datasets were then recomputed from the mean values of θ and q at each pressure level to give a consistent dataset. This procedure does not change the vertical structure of any of the variables, and for θ_E and θ_{ES} the difference between the average of the individual values and the recomputed averages is very small ($\approx$0.1 K). However, for T^*, p^* that have a more nonlinear relationship with θ and q, the extreme differences can be as large as 2 K and 10 mb.

Missing data have not been interpolated. The FGGE dropwindsondes do not give surface data, but usually data were available at 1000 mb (and occasionally at 1010 mb). Soundings with major data gaps were simply omitted from the smaller subset averages, and we believe the results presented here are not significantly affected by missing data. Objective interpolation of missing data is not straightforward because missing data were often at the top or bottom of the descent, or through the cloud and inversion layers, and could only be filled in by making assumptions about the atmospheric structure.

Some of the FGGE dropsonde data have questionable mixing ratios after the sonde passes through cloud (the relative humidity values do not fall below 93% again). Although there are a few of these in the datasets, they are too few to have much impact on the averages.

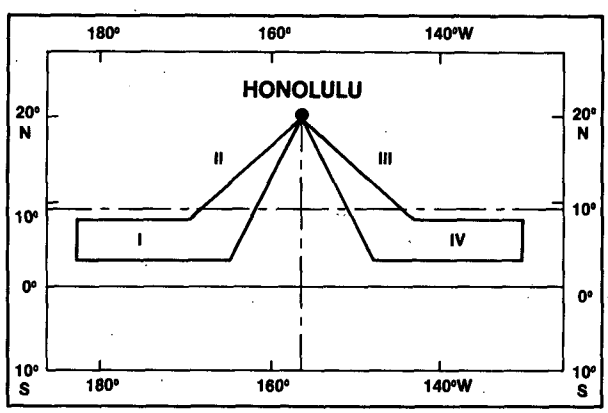

FIG. 1. Typical flight patterns during FGGE Special Observing Period 1 Pacific dropsonde missions, and data analysis regions I to IV.

c. *Conserved variable diagrams*

Figure 2 is an idealization to illustrate the usefulness of conserved variable diagrams. We show (dashed) a schematic mixing line (Betts, 1982) between the SPs of the mixed subcloud layer and the CBL top on a (θ_E, q_T) diagram. The q_T axis (which becomes the q axis for unsaturated air) has been reversed so that a sounding plotted on this diagram superficially resembles a more familiar (θ_E, p) plot. However, now both axes represent conserved variables in the absence of irreversible diabatic processes. The variables θ_E and q_T are particularly useful as coordinates. The condensation process does not change θ_E or q_T, but the precipitation process moves parcel points to lower q_T at constant θ_E (and the reverse for the evaporation of falling precipitation). The radiative process does not change q_T, but radiative cooling, for example, moves points to lower θ_E at constant q_T. Mixing lines are straight lines on this diagram, and advective processes do not move parcel points at all.

Consider the thermodynamic changes represented by the triangular path shown. Precipitation in the ascending deep convective branch of the tropical circulation moves parcels from the subcloud layer to lower q_T, at constant θ_E. Radiative cooling in the subsiding branch lowers θ_E at constant q_T. The air with the lowest θ_E sinks into the CBL, and its SP moves down the mixing line as it is mixed with air from below, on its final mean descent back into the subcloud layer. Note that while all these processes are associated with changes of parcel pressure in the atmosphere, Fig. 2 shows only the path of parcel (θ_E, q_T) (or SP), not the changes of parcel pressure. For a complete thermodynamic description we must label points on the diagram with their parcel pressure as well (see Fig. 5, for example).

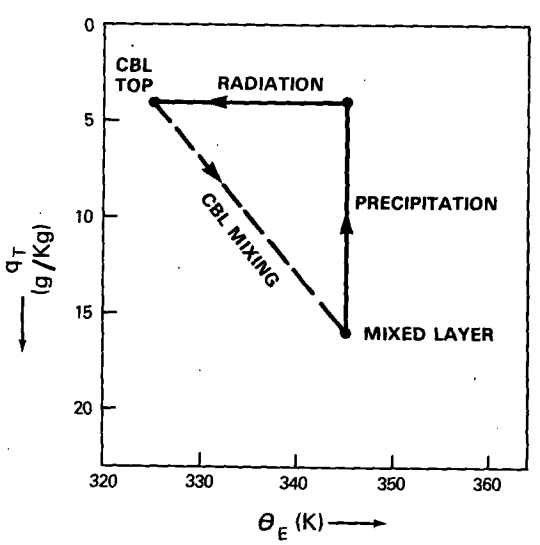

FIG. 2. Schematic θ_E–q diagram showing mixing line and effect of precipitation and radiative cooling on an air parcel saturation point.

3. Average soundings

a. *FGGE SOP-1, region IV*

This dataset comprised 84 soundings. We shall first present the average structure of this set before subdividing by inversion top pressure.

1) MEAN STRUCTURE

Figure 3 shows a plot of q, θ_V, θ_E and θ_{ES} (averaged at each pressure) against pressure from 1000 to 600 mb. Figure 4 shows p^* and $\mathcal{P} = (p^* - p)$ against pressure, where p^* is saturation level pressure. Negative values of $\mathcal{P}$ are related to the layer subsaturation. The typical three-layer structure (subcloud, cloud and inversion layers) of the CBL (Betts, 1975) is quite apparent in this mean dataset. Mean cloud base is around 965 mb (p^* for air at 1000 mb), and the subcloud layer has nearly constant θ_V. There is a distinct moist layer (the cloud layer) from 960 to 890 mb, which is unstable in θ_{ES} with a nearly constant value of $\mathcal{P} \approx -25$ mb [this corresponds to a relative humidity (RH) $\approx$ 88%]. The cloud layer is capped by the inversion layer, where θ_{ES} increases and where q and $\mathcal{P}$ have a greater decrease with height than in the layers below. The inversion top around 790 mb is marked by a maximum of θ_{ES} and a minimum of θ_E and $\mathcal{P}$. This minimum of $\mathcal{P}$ at the inversion top is a characteristic of this dataset that had not been anticipated. It implies that the $\mathcal{P}$ structure alone can be used to identify cloud base and inversion top and, with reasonable accuracy, the θ_E minimum at the inversion base (where $\mathcal{P}$ starts to decrease rapidly).

Figure 5 shows a conserved variable plot of mean saturation point against pressure (1000–600 mb) on a tephigram. This figure summarizes the vertical thermodynamic distribution (Betts, 1982). The subcloud layer data follows a θ_V isopleth (for unsaturated air); from a SL of p^* = 940 to 660 mb, the distribution is close to (but lies to the left of) a mixing-line structure (Betts, 1982), and at p^* = 660 mb there is a distinct change in gradient. This level corresponds to the top of the inversion (not the base) and marks the upper limit of convective mixing from the surface. The thermodynamic distribution in Fig. 5 can be projected onto an x–y plot of any pair of the tephigram coordinates p^*, θ, θ_V, θ_E, q. Although this presents no new information, it highlights different aspects of the SP distribution and facilitates the identification of characteristic thermodynamic signatures in more complex cases. Here we shall initially use the (θ_E, q) plot (discussed in section 2c) and later (section 4d) the (θ_V, p^*) plot.

Figure 6 shows the plot of θ_E against q for this average. As in Fig. 2 the mixing-ratio scale has been reversed so that the plot has some resemblance to a more familiar vertical θ_E sounding. The data points correspond to 10 mb levels in the atmosphere from 1000 to 600 mb. This type of conserved variable diagram

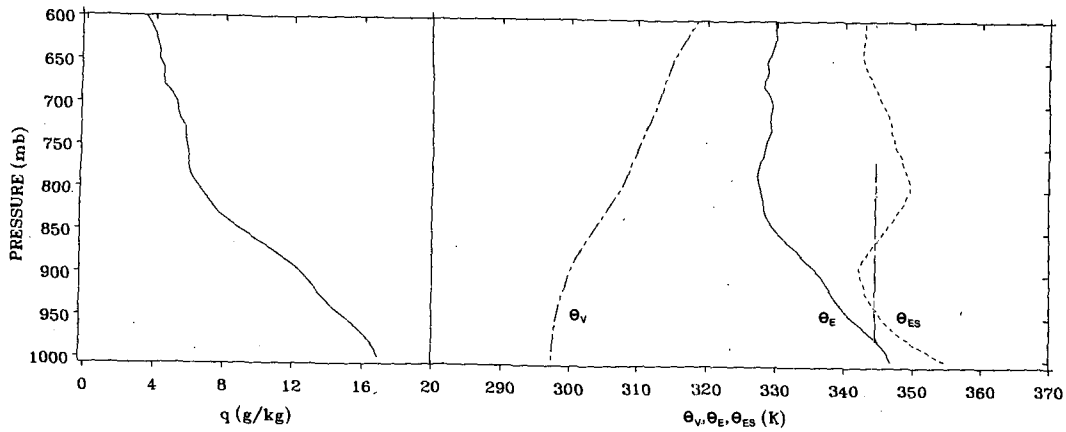

FIG. 3. Profile of q, θ_V, θ_E, θ_{ES} against pressure for FG14 average (FGGE, SOP-1, region IV, 84 soundings).

was revived by Paluch (1979) for the study of mixing processes in clouds, although Rossby (1932) much earlier used similar diagrams for the study of airmass structure. The pressure levels of the θ_{ES} minimum and maximum (corresponding to the base and top of the inversion) are marked. We see a slightly curved branch topped by a sharp kink at a level (780–790 mb) just above the θ_{ES} maximum (or inversion top) in Fig. 3. Mixing lines are straight lines in Fig. 6, so we see that, within the CBL, the structure approximates a mixing line. However, the sharpness of the kink in structure marking the top of the CBL was a surprise to us, and it will be explored further later.

Figures 3–6 show an average of 84 soundings, which have a range of CBL depths (inversion top heights). It is hard to present a meaningful variance for these averages, but scatterplots show some useful information.

2) SCATTERPLOT OF DATA

Figure 7 shows a (θ_E, q) scatterplot of the entire dataset whose mean structure is shown in Fig. 6. Figure 7 shows that the data divide into two groups. There is a broad, slightly curved branch within the CBL corresponding to the approximate mixing line structure in Fig. 6. A break is visible, and above the inversion is another block of data. The kinks in the mean (θ_E, q) plot (Fig. 6) appear here as an offset between the mixing line (extended to lower q) and the cluster of data above the CBL. We found this offset surprising because the mixing line represents the incorporation of air from the free atmosphere into the CBL.

Although the kink in Fig. 6 is at $q \approx 6$ g kg^{-1}, the break on Fig. 7 appears to be at a higher value of q. This is because Fig. 7 is composed of many individual

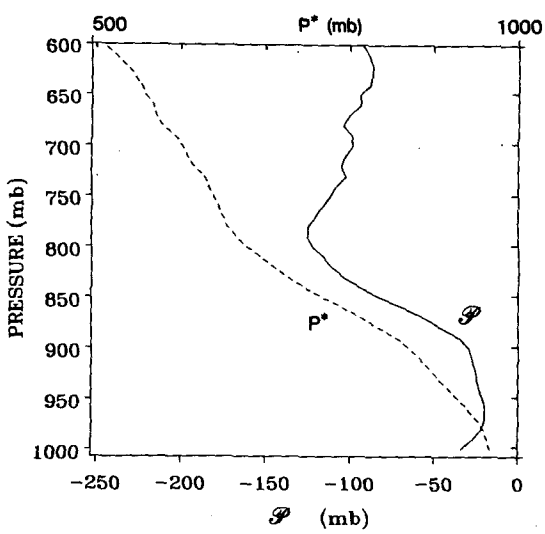

FIG. 4. As in Fig. 3 but for saturation level p^* (dashed) and $\mathcal{P} = p^* - p$ (solid).

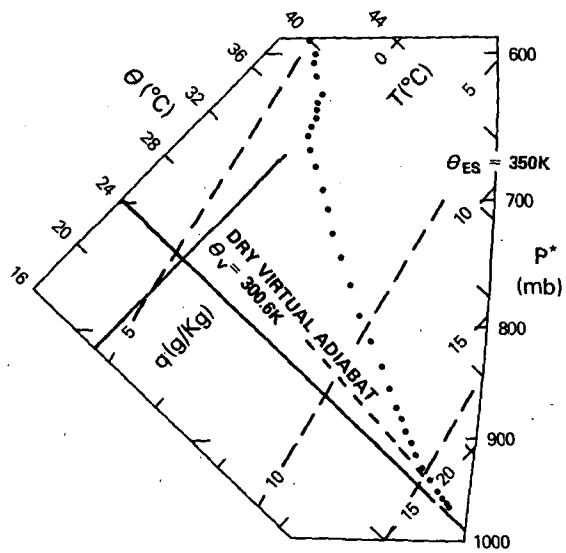

FIG. 5. Tephigram plot of air parcel saturation point for FG14 average.

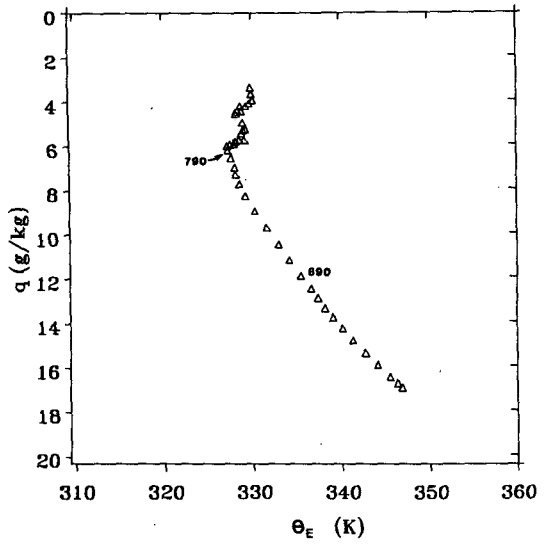

FIG. 6. Conserved variable plot of θ_E against q for FG14 average.

soundings, which each show a marked q reversal similar to the profile marked 141 in Fig. 10.

3) SUBDIVISION BY CBL DEPTH

We subdivided the 84 soundings by CBL depth into three classes using the pressure height of the inversion top. This was determined by examining each vertical profile for the pressure of the θ_{ES} maximum and the θ_E and $\mathcal{P}$ minima. These were usually within $\approx$10 mb of each other and gave an unambiguous determination of CBL depth to this accuracy. After rejecting some soundings with ill-defined inversions and some with extensive missing data, the remaining 58 were divided into three groups with inversion top heights in the 40 mb ranges (835–875, 795–835, 755–795), with 21, 25 and 12 soundings, respectively, in each category. Table 1 summarizes this and subsequent datasets. Figure 8 shows the profiles of mean θ_E and θ_{ES} for the three CBL depths. They all show a θ_E minimum and θ_{ES} maximum at the CBL top and a similar structure within the CBL, although FG143 (the deepest CBL) has a more stable θ_{ES} structure in the cloud layer. Figure 9 shows the $\mathcal{P}$ structure for the three averages. These all show the characteristic increase of $\mathcal{P}$ below cloud base, a rather flat region of approximately constant $\mathcal{P}$ below the inversion and a minimum $\mathcal{P}$ at the top of the CBL, corresponding to the minimum in θ_E and maximum in θ_{ES}. Figure 10 shows the (θ_E, q) plots for the three CBL depths. Points are again plotted for pressure levels every 10 mb from 1000 to 600 mb, with the pressure level of the inversion top and inversion base marked (the θ_{ES} maximum and minimum, respectively). The FG141 and 143 averages have been shifted $\pm$10 K in θ_E to the left and right, respectively, for clarity. The two shallow CBLs (FG141 and 142) show a quite similar mixing-line structure, with a marked kink at the CBL top. The deepest CBL (FG143) shows an indication of a change in ML slope just below 860 mb, which corresponds to the θ_{ES} minimum in Fig. 8. There is a slight change in slope between the cloud and subcloud layers (which can be seen more clearly in Fig. 29, discussed in section 4d).

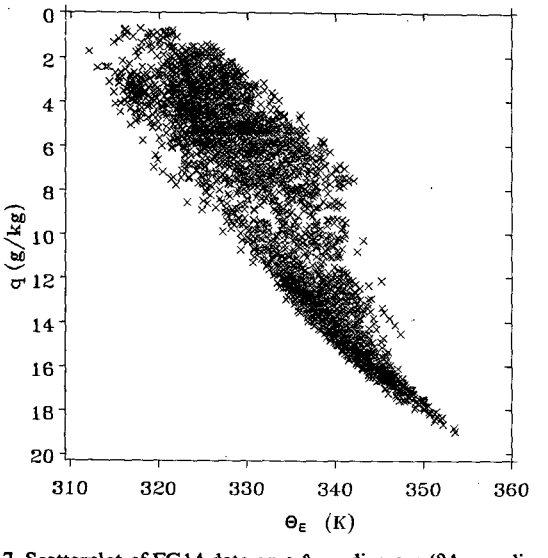

FIG. 7. Scatterplot of FG14 data on a θ_E–q diagram (84 soundings).

b. FGGE SOP I, region I

This dataset (FG11) comprised 42 soundings (only half as many as in FG14) from the western equatorial

TABLE 1. List of datasets.

Dataset	CBL top range (mb)	Number of sondes	Remarks
FG14		84	SOP-1, region IV, dropsondes
FG141	835–875	21	Subsets of FG14
FG142	795–835	25	
FG143	755–795	12	
FG11		42	SOP-1, region I, dropsondes
FG112	795–835	12	Subsets of FG11
FG113	755–795	16	
FG114	715–755	8	
FG113a	755–795	7	FG113 subset, double mixing line
FG113b	755–795	9	FG113 subset
PLANET	820–850	12	7–12 Feb 1969, structuresondes
BOMEX		approx. 180	22–24 June 1969, rawinsondes

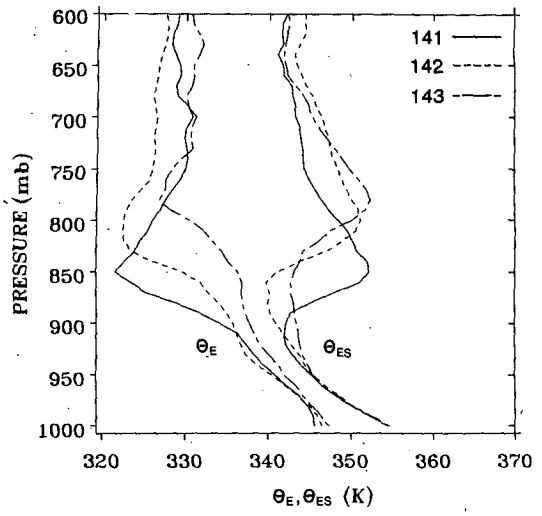

FIG. 8. Profiles of θ_E, θ_{ES} against pressure for FG141, 142, 143 averages.

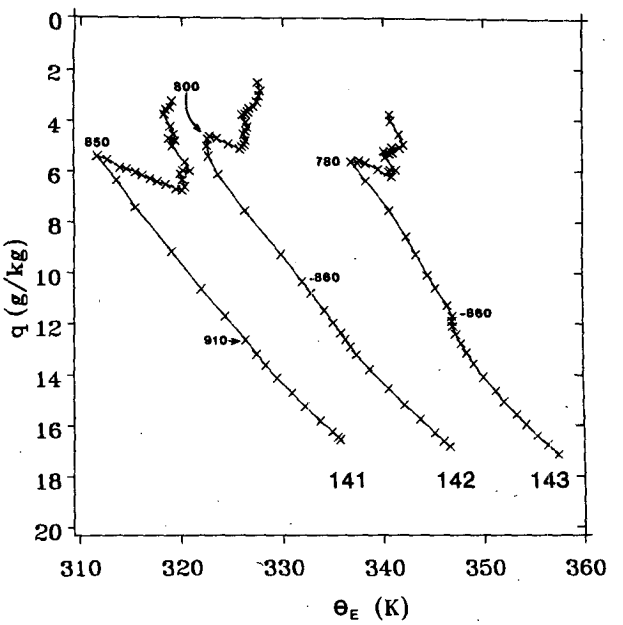

FIG. 10. The θ_E–q diagram for FG141, 142, 143 averages. FG141 (143) has been shifted −10 K (+10 K) in θ_E for clarity.

Pacific (region I in Fig. 1) during the first FGGE Special Observing Period. We first present the mean structure, which is similar to that shown in section 3 for the eastern Pacific (region IV), and then subdivide by inversion top pressure.

1) MEAN STRUCTURE

Figures 11 and 12 show the pressure average of the 42 soundings in this dataset (FG11). The mean structure is very similar to that shown in Figs. 3 and 4 for FG14. There are a few differences. For FG11 cloud base is higher (nearer 940 mb—Fig. 12) and the mean cloud layer from 940 to 850 mb is somewhat drier ($\mathcal{P} \approx -50$ mb). Figure 13 again shows a distinct kink at 790 mb in the (θ_E, q) plot corresponding to the mean CBL top, but unlike Fig. 6 there is a clustering of points and a slight change of structure near 850 mb, which corresponds to the θ_{ES} minimum, the top of the moist conditionally unstable layer.

The (θ_E, q) scatterplot (not shown) of this dataset is similar to Fig. 7. There is a separation between the band corresponding to the CBL mixing line and the data above the CBL.

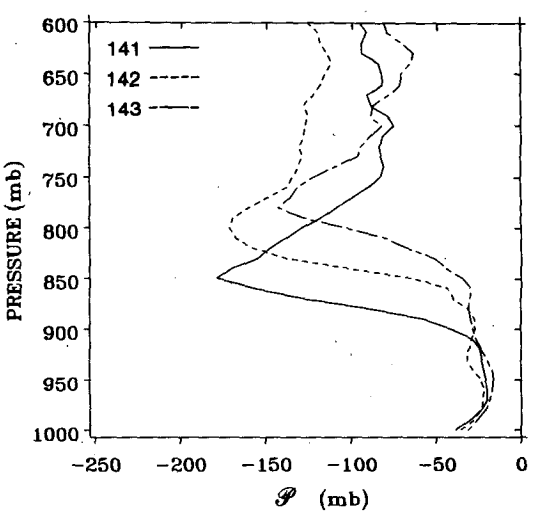

FIG. 9. As in Fig. 8 but for $\mathcal{P}$ profile.

2) SUBDIVISION OF FG11 BY CBL DEPTH

We estimated the CBL top for each sounding, as in section 3a, from the θ_{ES} maximum and the θ_E and $\mathcal{P}$ minima. This gave an unambiguous determination of CBL top for 36 out of the 42 soundings. These were divided into three groups in 40 mb ranges corresponding to CBL top pressures of 795–835, 755–795 and 715–755 mb, with 12, 16 and 8 soundings, respectively, in each group (see Table 1). Note that in contrast to dataset FG14 there were no sondes in the 835–875 mb shallow CBL category for this western Pacific dataset, and 8 were in a deeper category (715–755 mb).

Figures 14–16 are similar to Figs. 8–10. Figures 14 and 15 (as expected for the data selection procedure) show a θ_{ES} maximum, θ_E and $\mathcal{P}$ minimum at the inversion top. The structure in Fig. 15 again shows distinct subcloud and cloud layer structures. Figure 16 shows the (θ_E, q) structure for the three subsets. For clarity, the averages 114 and 112 have been offset ±10 K in θ_E. Average 112 has a structure very similar to 141 and 142 in Fig. 10. It shows close to a mixing line structure from the surface to 810 mb, and then a remarkable kink from 810 to 770 mb just above the CBL

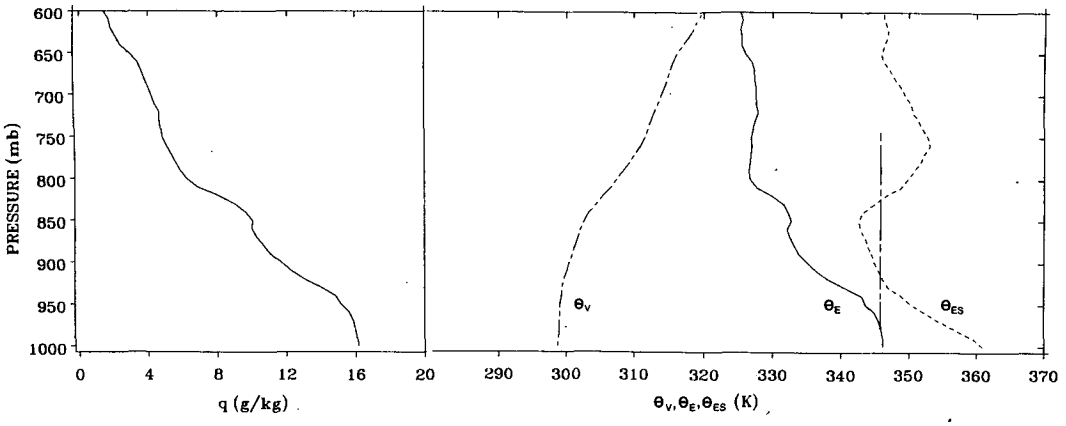

FIG. 11. Profile of q, θ_V, θ_E, θ_{ES} against pressure for FG11 average (FGGE, SOP1, region I, 42 soundings).

(the θ_{ES} maximum is at 800 mb). The deeper boundary layer averages 113 and 114 show a more complex structure. FG113 in particular shows a distinct double mixing line with a kink between 870 and 830 mb very similar to the kink at cloud top. FG114 has a similar transition with a clustering of points between 900 and 820 mb. For both averages 113 and 114, the θ_{ES} minimum is near 850 mb (see Fig. 13) in this region of transition between two distinct mixing lines. Comparison of Figs. 10 and 16 shows that the three averages (141, 142 and 112) with the lowest CBL top show a single mixing line through the cloud and inversion layers, but the three averages with a higher CBL top (143, 113 and 114) show a double structure with a transition near the top of the conditionally unstable cloud layer (the θ_{ES} minimum). Sections 4a and 4b will explore this further. We first will make a brief comparison with two earlier datasets.

c. *Comparison with ATEX and BOMEX*

The results from ATEX and BOMEX (both experiments in the Atlantic) have served as reference points for our present understanding of trade-wind boundary layer structure (Holland and Rasmusson, 1973; Nitta and Esbensen, 1974; Betts, 1975; Augstein et al., 1973, 1974). Consequently, it is useful to compare data from these experiments with the equatorial Pacific data discussed previously.

1) ATEX STRUCTURE

Figures 17–19 show an average of 12 sondes from an undisturbed period of ATEX from the ship *Planet* (7–12 February 1969). Two averages are shown. The solid lines in Figs. 17 and 18 (labeled PLANET) are the θ_E, θ_{ES} and $\mathcal{P}$ profiles computed by averaging the

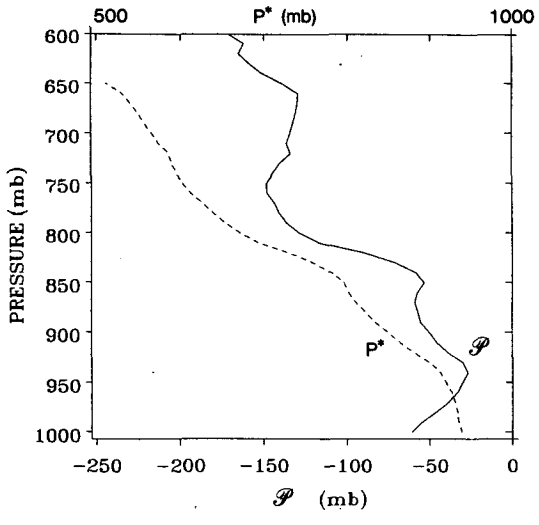

FIG. 12. As in Fig. 11 for p^* and $\mathcal{P}$.

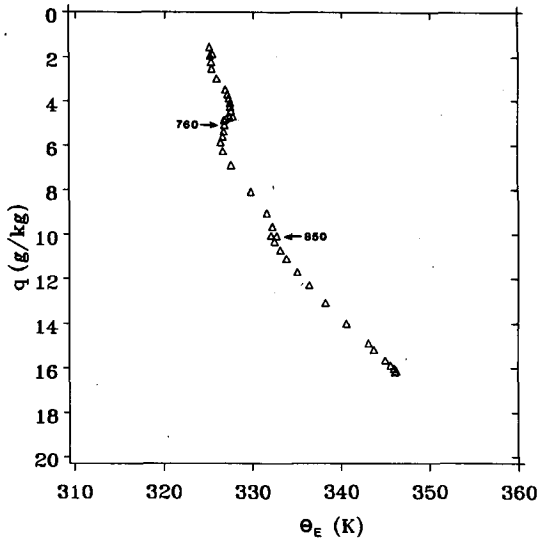

FIG. 13. The θ_E–q diagram for FG11 average.

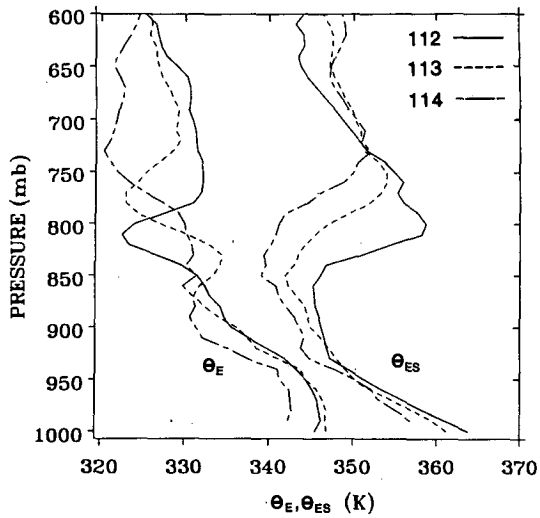

FIG. 14. Profile of θ_E, θ_{ES} against pressure for FG112, 113, 114 averages.

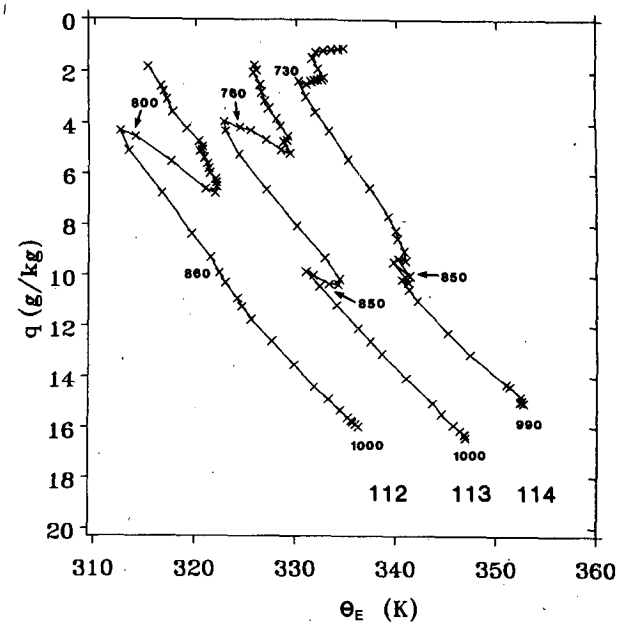

FIG. 16. The θ_E–q diagram for FG112, 113, 114 averages. FG112 (114) has been shifted −10 K (+10 K) in θ_E for clarity.

individual soundings at 10 mb pressure levels as in sections 3a and 3b. This set of soundings had CBL tops between 820 and 850 mb. The dashed lines (labeled AUGSTEIN) denote the average structure from Augstein et al. (1974). The Augstein et al. (1974) structure was found by first selecting points at the top of the mixed layer, transition layer at cloud base, inversion base and inversion top and then averaging p, θ and q at these levels. This averaging method preserves the sharp inversion gradients, although it is a little more subjective.

The θ_E, θ_{ES} and $\mathcal{P}$ structures (Figs. 17, 18) are similar to those shown earlier. The ATEX inversion is stronger than those for the FGGE cases, and the cloud layer below the inversion is much closer to saturation. Although the 10 mb average smoothes the profiles at the inversion relative to the Augstein et al. profile, both show essentially the same structure.

Figure 19 shows the θ_E–q plot. It is very similar to Figs. 10 and 16, with a small change of slope between cloud and subcloud layers, and a sharp kink at the inversion top with a layer above of almost constant q. There is no data above 700 mb. Augstein's average shows that the mixing-line slope through the cloud and inversion layers is maintained right up through the in-

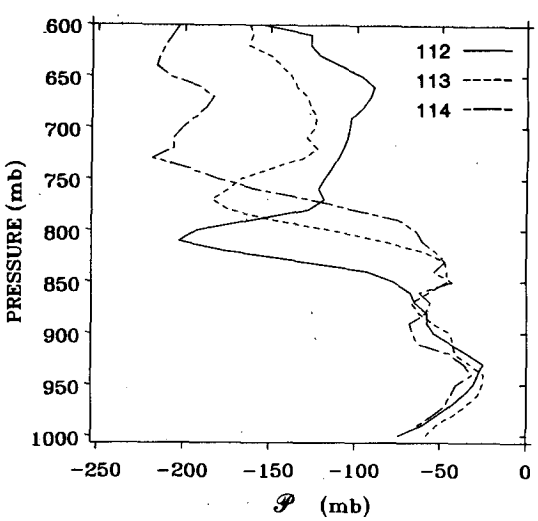

FIG. 15. As in Fig. 14 for $\mathcal{P}$ profiles.

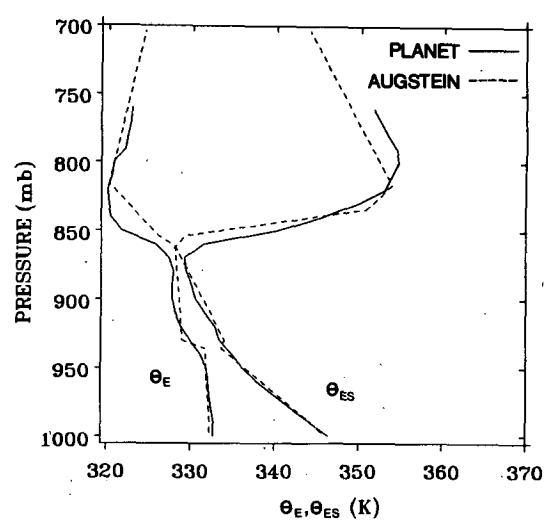

FIG. 17. Profiles of θ_E, θ_E against pressure for PLANET averages.

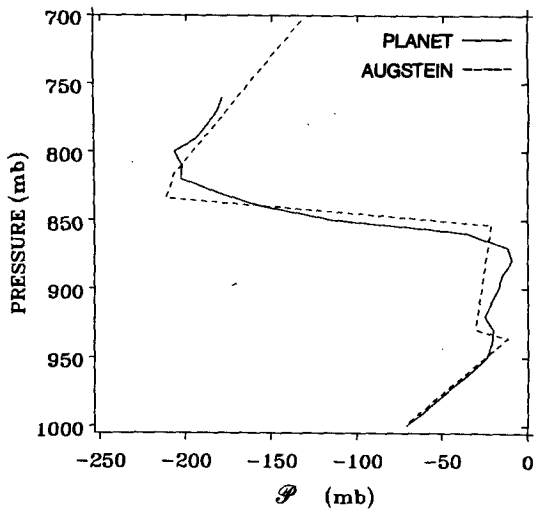

FIG. 18. As in Fig. 17 for $\mathcal{P}$ profile.

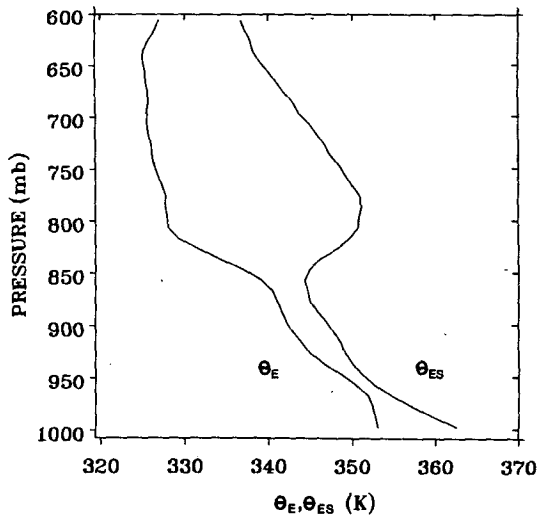

FIG. 20. Profile of θ_E, θ_{ES} against pressure for BOMEX average.

version to 834 mb. The subcloud layer has almost constant θ_V (not shown).

2) BOMEX STRUCTURE

Figures 20–22 show the structure of a three-day undisturbed average from BOMEX (22–24 June 1969). (Values are plotted every 10 mb below the mean surface pressure of 1016 mb.) Figure 20 shows the θ_E and θ_{ES} profiles typical of a CBL with top near 800 mb. Figure 21 shows the $\mathcal{P}$, p^* structure (with $\mathcal{P} \approx -20$ mb in the cloud layer 950–840 mb) and a rapid decrease through the inversion to a flat minimum above the CBL. Figure 22 shows the θ_E–q plot. The mixing line through the cloud and inversion layers is present, as in earlier figures, but in contrast to Figs. 6, 10, 13, 16 and 19, the minimum θ_E and sharp kink in the profile is not at the top of the CBL, but nearly 150 mb higher at $p \approx 640$ mb. Indeed, at the top of the inversion (790 mb) only a small discontinuity is visible in the (θ_E, q) plot. We shall discuss this further in the next section.

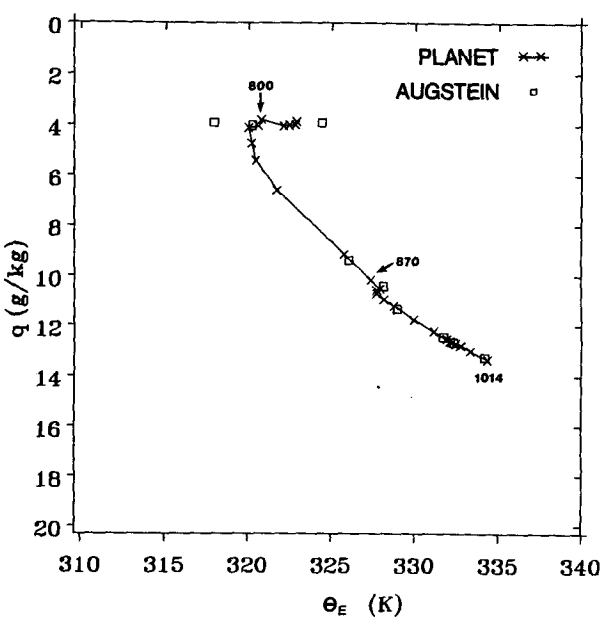

FIG. 19. The θ_E–q diagram for PLANET averages.

4. Discussion of CBL structure

a. Characteristic CBL structures

A distinct picture emerges for the structure of the CBL. In particular, we have established the usefulness of four possible criteria for the thermodynamic depth

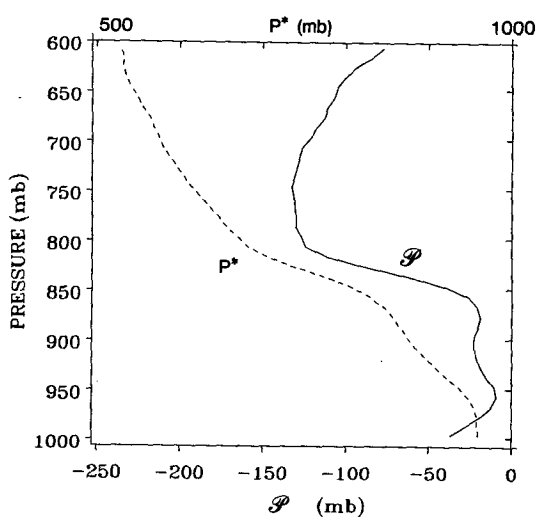

FIG. 21. As in Fig. 20 for p^*, $\mathcal{P}$ profiles.

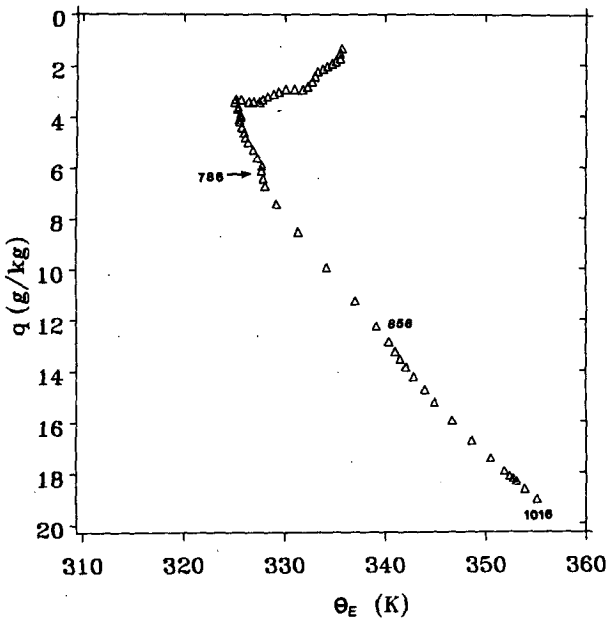

FIG. 22. The θ_E–q diagram for BOMEX average.

of the CBL. The CBL has a characteristic ML structure up through the cloud and inversion layers to the top of the CBL. This is the layer that is coupled thermodynamically to the surface. The top of this ML structure is typically characterized by a maximum in θ_{ES} and a minimum in θ_E and $\mathcal{P}$. The air above the CBL is not coupled thermodynamically to the surface and is usually sinking with radiative cooling, and consequently decreasing θ_E. The air *just* above the CBL has, in some sense, been cooling and sinking the longest (see section 4f) and reached the lowest θ_E (Betts, 1985) before it enters the CBL and becomes coupled to the surface.

Only one of the averages does not fit this picture. The BOMEX average (Fig. 22) shows a continuation of the decrease of θ_E with height above the low-level trade inversion. This suggests that at some time in the history of this air mass, convection had reached deeper levels. For this average we do not have the individual soundings, but possibilities for this structure can be suggested. The BOMEX array was in an east-northeasterly trade-wind flow from the surface to 650 mb. It is likely that we are seeing simply the remains of the deep Saharan boundary layer, which often extends to 650 mb (Carlson and Prospero, 1972) and typically has values of $\theta \approx 313$ K and $q \approx 4$ g kg^{-1} (giving $\theta_E \approx 326$ K). In contrast, for the ATEX dataset the flow above the inversion is from the southeast (Augstein et al., 1973) and probably has a different history. However, we note also that, unlike the FGGE averages, the mean BOMEX subcloud θ_E of 353 K exceeds the θ_{ES} maximum at 790 mb of 351 K (Fig. 20), so that there may have been intermittent convection in regions of mesoscale organization, which has penetrated the trade inversion.

b. CBL internal structure

We noted in section 3b that three of the FGGE averages (FG141, 142 and 112: those with CBL tops in the range 875–795 mb) showed a single mixing line on a (θ_E, q) plot (Figs. 10 and 16) through the cloud and inversion layers. The ATEX and BOMEX averages that have CBL tops at ≈820 and 806 mb, respectively, are similar. However, the three deeper CBL averages (FG143, 113 and 114, which have CBL tops in the range 795–715 mb) show a distinct double structure with a kink near the θ_{ES} minimum (the top of the conditionally unstable cloud layer) and a second mixing line above through the inversion layer. This suggests that once the CBL reaches a certain depth a new physical process becomes important, and an obvious possibility is that the deepest clouds, which penetrate the inversion, start to precipitate, while a population of smaller clouds, which do not precipitate, continue to mix the conditionally unstable layer. Studies by Byers and Hall (1955) and Ludlam (1980) showed that some clouds over the tropical oceans start to precipitate once their tops reach above 2 km, which would correspond approximately to 800 mb.

c. Double mixing-line structure

Figure 16 for the FG113 average shows a distinct double mixing-line structure with a small q reversal around 850 mb, very similar to that at 770 mb, the top of the CBL. Closer examination of this subset of 16 sondes shows that this structure is a marked feature of 7 of the soundings, and so a further subdivision was made into two groups: 113a (7 soundings) and 113b (9 soundings). The differences between these two averages are interesting.

Figures 23–25 compare these two averages. Figure 23 shows that although both have similar surface and

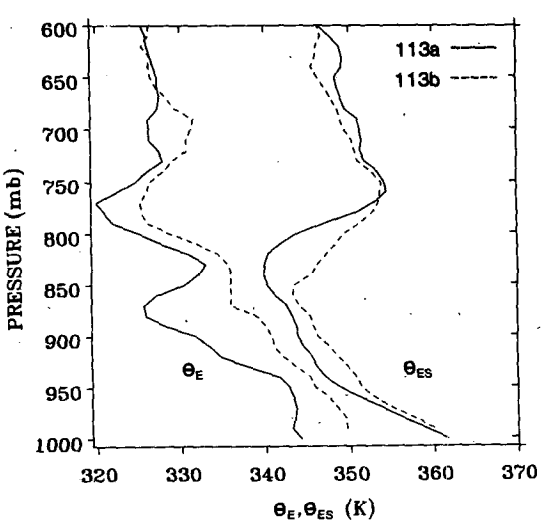

FIG. 23. Profiles of θ_E, θ_{ES} against pressure for FG113a, 113b averages.

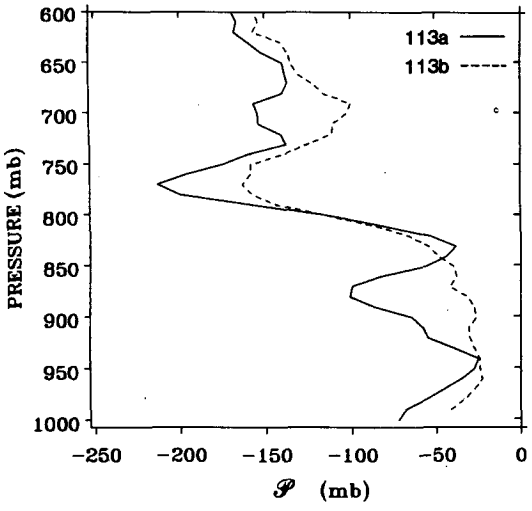

FIG. 24. As in Fig. 23 for $\mathcal{P}$ profiles.

inversion top values of θ_{ES}, 113a is much cooler in the CBL and has a drier subcloud layer (lower θ_E) and higher cloud base (Fig. 24). Although 113b has a structure typical of earlier averages, 113a has a second minimum in θ_E and $\mathcal{P}$ at 875 mb, which corresponds to a weak stable layer of nearly constant $\theta_{ES} \approx 343.5$ [Fig. 23, very close to the subcloud θ_E (dashed line)]. The (θ_E, q) plots (Fig. 25) for the two averages show a remarkable difference. Set 113a shows two mixing lines with a marked q and θ_E reversal from 870 to 830 mb as well as the CBL top of 770 mb (the θ_{ES} minimum at 840 mb is marked). Set 113b shows only a kink around the same pressure similar to datasets 114 and 143. The subset 113a thus seems to have a much more pronounced double boundary layer structure.

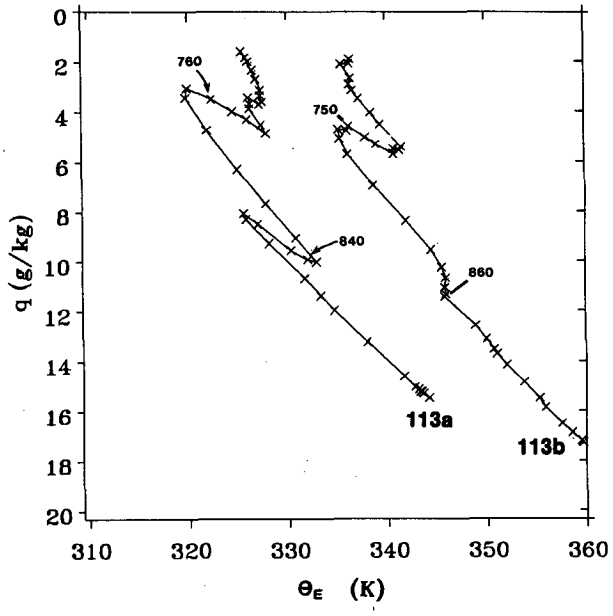

FIG. 25. The θ_E–q diagram for FG113a, 113b averages (FG113b has been shifted +10 K).

We do not understand how the double mixing-line structures seen in the soundings in the FG113a average are produced, but we can speculate on possible mechanisms. Differential horizontal advection of boundary layers of different depths near the equator is a possibility. However, the wind data has poor vertical resolution, and adequate horizontal moisture fields are not available for this region for detailed analysis.

The presence of these double structures and the kinks at the CBL top both involve reversals in the θ_E and q gradients with height, and it seems worthwhile to discuss prototype processes that could modify a ML structure. The q minimum at the CBL top is particularly prevalent and has been seen by others (Lenschow, Khalsa and Hanson, personal communications, 1986).

A mixing-line structure is produced when the vertical convection mixing dominates over processes that do not conserve air parcel SP, such as radiative cooling or the processes of precipitation and evaporation of falling rain. Schematically, we might consider a mixing line on a (θ_E, q) plot being modified by these two processes as in Fig. 26.

Precipitation falling from an *upper* cloud layer and evaporating *below* can warm the upper layer and cool the lower one. This is a restratification that uncouples the CBL into two layers, which might continue to be mixed internally. Nicholls (1984) observed this uncoupling in stratocumulus over the North Sea and attributed it both to evaporation below cloud base and reduced radiative cooling in the daytime due to solar absorption in the upper cloud layer. The FGGE soundings are daytime soundings. The precipitation–evaporation couplet, which closely conserves θ_E, does not produce either a θ_E or q reversal between the two layers. It could split a single mixing line (light solid) into two with a step in q (heavy solid line in Fig. 26)

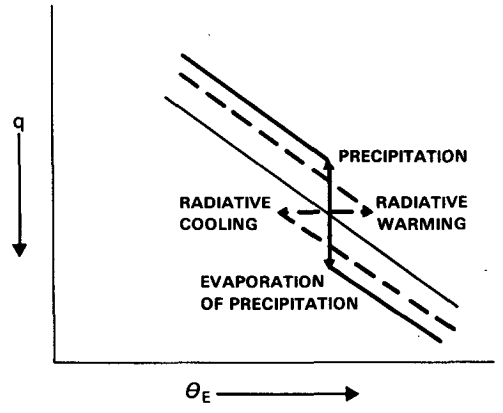

FIG. 26. Schematic showing modification of a mixing line by different radiative heating/cooling rates, and precipitation/evaporation couplet.

because the precipitation (evaporation) process moves SPs at the constant θ_E to lower (higher) q. This resembles the structure seen in Figs. 10 and 16 for datasets 143 and 114.

Radiative uncoupling that conserves q, but not θ_E, could produce a θ_E reversal between two layers (shown dashed in Fig. 26), but not a q reversal. Thus, neither process can explain the q and θ_E reversal that we see in Fig. 25 (from 870 to 830 mb) and at the CBL top in most averages (and the individual soundings). If these structures are produced locally, rather than by differential horizontal advection of separate CBLs, then a more complex process is needed. Two related aspects need explanation. How do the distinct layers (in Fig. 25) remain separate? How is the dry air (seen at 870 mb) brought down into the lower layer? A continuous hierarchy of cloud sizes would probably smear out any internal structure in the CBL, so the maintenance of two separate layers suggests the possibility of two distinct cloud populations. It is possible that intermittent cumulus convection (in time or space), with precipitating updrafts and penetrative downdrafts driven by evaporation of precipitation, might produce this structure.

Figure 27 shows a schematic reconstruction using average 113a (from Fig. 25). Patches of energetic cumulus can penetrate the weak stable layer at 880 mb and inject moisture into the upper layer. If they precipitate before mixing, the injected air will have an SP shifted up the moist adiabat relative to the subcloud air. The dotted lines in Fig. 27 are θ_V isopleths. Point A represents the properties of an updraft parcel that has precipitated and that will give neutrally buoyant mixtures at 830 mb after evaporating its remaining cloud water. We suppose that this precipitation is carried to near the CBL top, where it falls out and evaporates *rapidly* into the very dry air, at 790 mb, shifting the SP of this air down a moist adiabat and cooling it sufficiently to sink in a penetrative downdraft into the lower layer to θ_V equilibrium at, say, 870 mb (point B). It can then mix with the environment and act as a "source" of dry, low θ_E air. These updrafts and downdrafts must penetrate without thoroughly mixing with surrounding air, or the two-layer structure will rapidly be eliminated, so the suggested mechanism may require some organization on the cloud scale or mesoscale.

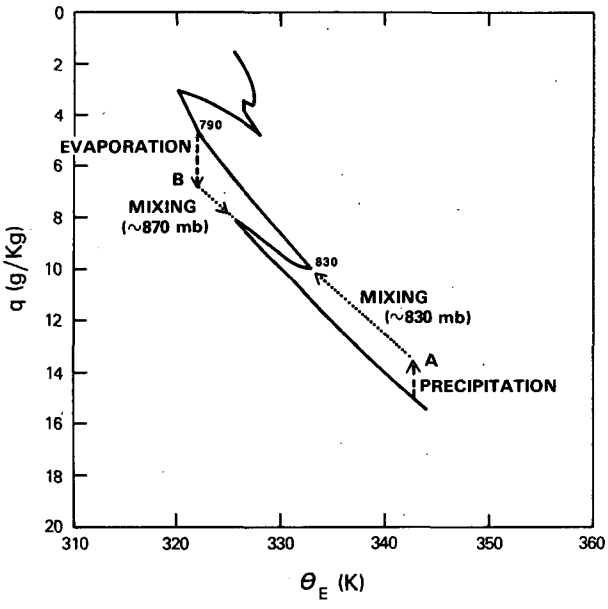

FIG. 27. Schematic showing double mixing-line structure and effect of precipitation (evaporation) and mixing on updraft (downdraft) SP paths. Dotted lines are dry virtual adiabats (constant θ_V).

The underlying reason why this mechanism exists is related to the slope of the ML, the θ_V isopleth (the dotted line in Fig. 27) and the moist adiabat. The mixing process is constrained to move SPs along the MLs in Fig. 27, but the precipitation and evaporation processes move SPs along the moist adiabat (constant θ_E). The slope ($\partial\theta_V/\partial p^*$) of the mixing line is approximately half that of the moist adiabat, so that evaporation of precipitation can alter the equilibrium level of an air parcel in the CBL (which depends on θ_V) with only half the increase in p^* when compared with the mixing process. Thus, air in an evaporatively driven penetrative downdraft can change its θ_V equilibrium level and bring down air from above with relatively low p^* (and low θ_E) to give the local q and θ_E minima at 870 mb that we see in Fig. 27. That is the physical consequences differ, depending upon whether cloud towers evaporate their liquid water by mixing with dry (inversion-level) air or the droplets first precipitate into dry air before evaporating.

Figure 28 shows a schematic of the cloud and downdraft air flow for the deep and shallow cloud population, adjacent to the θ_E and θ_{ES} profiles, which illustrates these two possibilities. The shallow nonprecipitating clouds overshoot and have a single downward circulation as they mix and evaporate their cloud water (Betts, 1973). Likewise, if the overshooting cloud towers of the deeper clouds, which penetrate the inversion, do not precipitate, they, too, will produce a single downward circulation. This is shown dashed in Fig. 28. If, however, these clouds precipitate before mixing, this splits the downward circulation into two separate branches as shown. The fallout of precipitation (marked P) reduces the cloud water so that the cloudy air, as it mixes, cools less and does not sink as far as the dashed trajectory. This air sinks to near the inversion base and is the source of the cool moist air (high θ_E, low θ_{ES}) at this level. The precipitation evaporates (marked E) into the very dry air in the inversion, cooling it (with a relatively large fall of θ_V, but a relatively small increase of p^*), and driving a dry penetrative downdraft, which has an equilibrium level well below the inversion base. This air can form the dry capping layer for the shallow clouds. This same mechanism

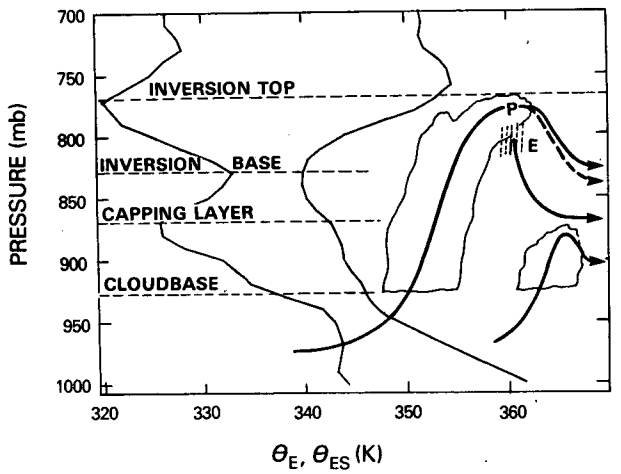

FIG. 28. Schematic air parcel paths through two sizes of cloud showing origin of moist layer at base of inversion (830 mb) and dry layer (870 mb) capping the smaller cloud population. On the left are θ_E, θ_{ES} plots for the FG113a average.

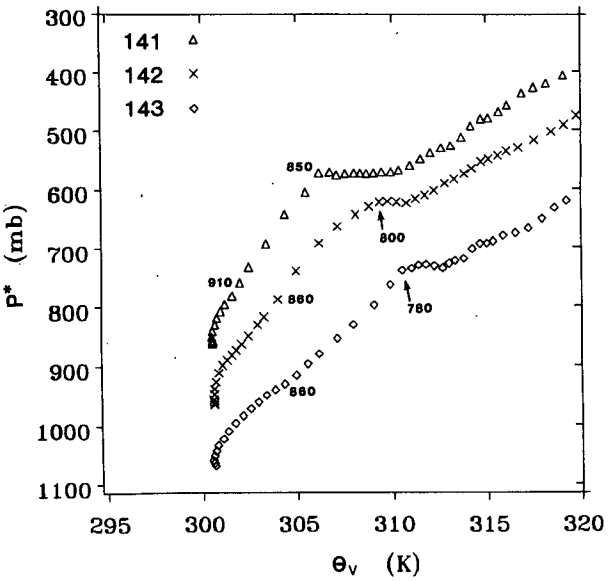

FIG. 29. The θ_V–p^* diagram for FG 141, 142, 143 averages. FG141 (143) has been shifted −100 mb (+100 mb) in p^* for clarity.

(with a little more mixing!) could also be producing the θ_E–q profiles in the sets FG143, 113b and 114, which just show a step in q (at constant θ_E) between a lower and upper mixing line.

If such a mechanism exists, then it may play a role above the CBL in producing reversals of the mean q gradient. Locally deeper cumulus congestus, organized perhaps on the mesoscale, could inject moisture into higher levels and bring down relatively drier air by evaporatively driven downdrafts. A related possibility is that the q reversals above the CBL might be produced by a similar mechanism in a region of precipitating convection and might have been preserved as the air subsided during several days.

d. Mixing-line stability

In this section we shall show θ_V and p^* plots for some of the average datasets. Although these, in principle, contain no more information than the θ_E–q plots, they highlight a different aspect—the stability of the conserved variable distribution (Betts, 1982, 1983). Figure 29 shows the three subsets FG141, 142 and 143, and Fig. 30 shows FG112, 113 and 114. Because these distributions lie almost on top of each other, they have been shifted ±100 mb in p^* for clarity. We see that the cloud and subcloud layers have a quite different gradient. The subcloud layer has almost constant θ_V (although it has a gradient of p^*). There is a characteristic gradient through the cloud and inversion layers (the kink near 850 mb is only visible on set 113), and the layer above the inversion top is characterized by a change of θ_V at nearly constant p^*. The neutrality of the subcloud layer to θ_V is no surprise. Although the averages are not well mixed in the subcloud layer, they show an SP distribution along a dry virtual adiabat, the neutral buoyancy reference process for unsaturated convection. The ATEX and BOMEX data are similar (not shown).

Betts (1982, 1985) has suggested that the slope of ML in the cloud layer is controlled by the SP of air sinking into the CBL through the inversion top. Figures 29 and 30 support this concept. However, the air at the CBL top, which is at the base of the constant p^* layer in these figures, is also the air with the minimum q, so the origin and structure of the layer above the CBL top is of great importance in modeling.

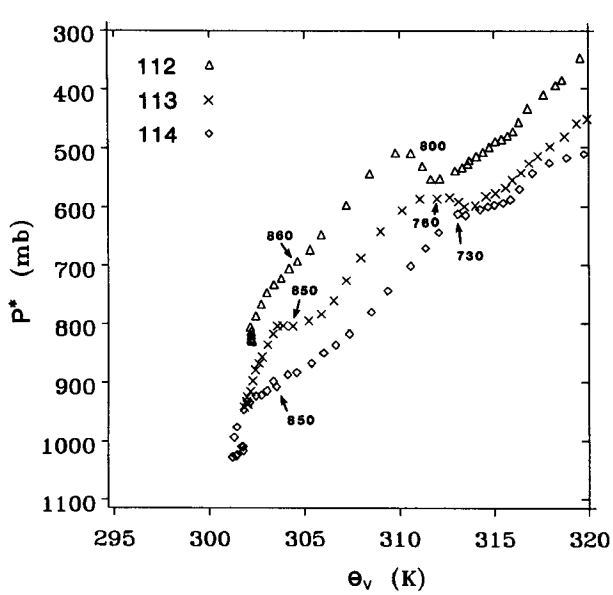

FIG. 30. The θ_V–p^* diagram for FG 112, 113, 114 averages. FG112 (114) has been shifted −100 mb (+100 mb) in p^* for clarity.

e. Origin of CBL top air

In parameterizing the CBL in global circulation models, the computation of mixing-line slopes ($\partial\theta_V/\partial p^*$ or $\partial\theta/\partial p^*$) has an important control on the surface Bowen ratio for oceanic conditions (Betts and Miller, 1985). We have already mentioned that the q minimum at the CBL top is hard to explain, although it seems very widespread in this and other FGGE datasets (not shown in this paper). We do not known whether the q reversal above the CBL is produced locally, for example, by mesoscale organization of convection coupled with the downdraft process discussed in section 4c, produced by differential horizontal advection over considerable distances, or subsided from a source in a region of precipitating convection. It is clear that the air above the CBL has been in a subsiding circulation for several days, and we speculated that there might be a radiative mechanism that could cause dry air to sink faster and so reverse the q gradient. However, sample calculations show that, given an inhomogeneous q distribution, the infrared cooling rate of dry patches is likely to be less than that of moist patches. The q minimum air has also been observed to have a maximum ozone concentration (Lenschow, personal communication, 1986), suggesting a possible origin at a higher level in the troposphere, but the ozone is insufficient to affect its radiative cooling rate. Thus, we are still looking for convincing mechanisms to explain the q reversal above the CBL top.

Figures 29 and 30 show that there is a layer of almost constant p^* just above the CBL. This layer has also almost constant T^* (not shown). The origin of this air is of interest. Table 2 shows the thermodynamic parameters of the 10 mb layer at the CBL top that has the lowest θ_E. The BOMEX data is for the level of θ_{ES} maximum, since this average does not have a θ_E minimum near the CBL top. If we *assume* this air has sunk with radiative cooling, but without *mixing or* precipitation evaporation, we can estimate its level of origin by using conservation of q, provided we also know the vertical q structure of the atmosphere where this air originated. This is conceptually similar to the method used (e.g., Zipser, 1969; Betts 1976) to estimate the level of origin of precipitation-driven downdrafts using θ_E conservation. Table 2 shows the average of sets FG112, 113, 142, 143 (marked with an asterisk), which have similar parameters. A set of parameters is given for the pressure level (573 mb), where a disturbed atmosphere average (estimated from the Firestone and Albrecht, 1986, averages for the corresponding disturbed FGGE regions) crosses the $q = 4.7$ g kg^{-1} isopleth. The difference between these two suggests that the CBL top air has subsided approximately 216 mb, while cooling 10.9 K in potential temperature. At a radiative cooling rate of $\theta_R = -1.75$ K day^{-1} this corresponds to six days of subsidence at 35 mb day^{-1}. In a later paper we shall attempt a more detailed thermodynamic analysis of the balance among subsidence, radiation and convection for these FGGE averages.

It is clear from Table 2 and this computation that for all the datasets, except FG114, the air at the CBL top has subsided from a level just above the freezing level in the mean tropical atmosphere (assuming that it has conserved its q during the descent).

f. Modification of $\mathcal{P}$ during descent

The calculation in Table 2 also illustrates why the air at the CBL top has a maximum negative value of $\mathcal{P} = p^* - p$. Following a parcel as it sinks with radiative cooling, both p and p^* are changing

$$\dot{\mathcal{P}} = \dot{p}_R^* - \dot{p} = \dot{p}_R^* - \omega. \quad (1)$$

TABLE 2. SP parameters for low θ_E air at CBL top.

Dataset	p (mb)	T^* (°C)	p^* (mb)	θ (K)	q (g kg^{-1})	θ_E (K)	$\mathcal{P}$ (mb)
*FG112	810	−5.2	608	309.0	4.3	322.6	−202
*FG113	770	−6.7	587	310.4	4.0	322.9	−183
FG114	730	−15.0	512	312.7	2.3	320.0	−218
FG141	850	−0.8	672	305.2	5.4	321.7	−178
*FG142	810	−2.5	643	307.1	5.0	322.6	−167
*FG143	780	−1.1	638	309.5	5.6	326.9	−142
PLANET	800	−7.1	594	308.8	3.8	320.8	−206
BOMEX	786	0.6	656	308.8	6.1	327.7	−130
*Averages	793	−3.8	619	309.0	4.7	323.8	−174
Disturbed atmosphere	577	−5.6	535	319.9	4.7	335.3	−42
						days	mb day^{-1}
Difference	216 Δp	−1.8 ΔT^*	84 Δp^*	−10.9 $\Delta\theta$	0 Δq	−11.5 $\Delta\theta_E$	−132 $\Delta\mathcal{P}$	6.2 Δt	34.7 ω

The radiative change of saturation level is given by

$$\dot{p}_R^* = -\dot{\theta}_R/(\partial\theta/\partial p)q_S. \quad (2)$$

For the mean descent in Table 2, $(\partial\theta/\partial q)q_S = -13.1$ K/100 mb, which gives (for $\dot{\theta}_R = -1.75$ K day^{-1})

$$\dot{p}_R^* = 13.4 \text{ mb day}^{-1}$$

and $\dot{\mathcal{P}} = 13.4 - 34.7 = -21.3$ mb day^{-1}, in agreement with the change in Table 2 for a descent taking 6.2 days.

Equation (1) can be written in another form. Substituting (2) and $\omega = -\dot{\theta}_R/(\partial\bar{\theta}/\partial p)$, where $\partial\bar{\theta}/\partial p$ is the mean stratification, gives

$$\dot{\mathcal{P}} = \dot{\theta}_R/[(\partial\theta/\partial p)q_S - (\partial\bar{\theta}/\partial p)]. \quad (3)$$

We see that if $(\partial\theta/\partial p)q_S \approx -13$ K/100 mb and $\partial\bar{\theta}/\partial p \approx -5$ K/100 mb for the tropical atmosphere, then

$$\dot{\mathcal{P}} = 12.5\,\dot{\theta}_R \text{ mb day}^{-1}$$

if $\dot{\theta}_R$ is in K day^{-1}. We see that the longer air subsides, the more negative its value of $\mathcal{P}$ will become. The minimum value of $\mathcal{P}$ seen at the top of the CBL reflects the fact that this air has in some mean sense subsided the longest.

5. Parametric modeling of internal CBL structure

The mixing line parameterization for the CBL suggested by Betts (1985, 1986) determined the ML slope by mixing air near the surface with air above the CBL top and specified the distribution of SP within the CBL along this ML using an empirical parameter β, defined as

$$\beta = dp^*/dp = d\mathcal{P}/dp + 1. \quad (4)$$

In this section we shall discuss how well the dataset averages fit this model and extract values for β.

a. Subcloud layer

It is clear from the (θ_V, p^*) averages [Figs. 29, 30 and BOMEX, ATEX (not shown)] that the subcloud layer SP distribution follows a dry virtual adiabat (constant θ_V) rather than the CBL top mixing line. Table 3 shows the range of values with a mean (subcloud) $\beta_{SC} = 0.42 \pm 0.15$ for the eight subsets FG112, 113, 114, 141, 142, 143, BOMEX and PLANET. Since $\beta = 0$ represents a well-mixed layer, these values suggest the subcloud layer is not well mixed. Although this is true, subjective inspection of the individual soundings suggests that this average of β is somewhat of an overestimate for the undisturbed mixed layer because of variations in cloud base in the soundings (β is larger in the cloud layer) and the presence of a few soundings with questionably high humidities $\approx 95\%$ in the subcloud layer (which have $\beta \approx 1$). These high humidities are probably due to the humidity sensor not recovering after descending through cloud. For parametric modeling of the subcloud layer structure, we recommend using $\beta_{SC} = 0.3$ and θ_V constant.

b. Cloud and inversion layers

Figures 10, 16, 19 and 22 show that the shallower CBLs fit the simple mixing-line model quite well through the cloud (cloud base to θ_{ES} minimum) and inversion layers (θ_{ES} minimum to CBL top). The deeper CBLs (FG143, 113 and 114) show a distinct change in mixing line roughly between the cloud and inversion layers. [The pressure level corresponding to the θ_{ES} minimum (usually 850–860 mb) is marked in Figs. 10 and 16.] We suggested in section 4 that this might be due to the onset of precipitation in the deepest clouds (which penetrate into the inversion) once the highest tops reach about 790 mb. Clearly, an improved parametric model should account for this double mixing-line structure in deeper CBLs.

Table 3 shows values of β_C, B_I for the cloud and inversion layers for the eight averages and their mean. Here Γ_C is the mixing-line slope $(\partial\theta_V/\partial p^*)$ computed from cloud base to the θ_{ES} minimum and Γ_{CI} that computed from cloud base to the CBL top. Table 3 shows typical values of $\beta_C \approx 1.2$ for the cloud layer and $\beta_I \approx 3$ for the inversion layer. There is some suggestion in the FGGE data that with increasing CBL depth, β_I and perhaps β_C decrease. The two estimates

TABLE 3. CBL parameters.

Dataset	β_{SC}	β_C	β_I	CBL top (mb)	Γ_C (K/100 mb)	Γ_{CI} (K/100 mb)	Γ^+ (K/100 mb)	R_C	R_{CI}
FG112	0.30	1.60	3.7	810	−2.2	−2.6	−4.1	0.54	0.63
FG113	0.35	1.21	3.5	770	−2.0	−2.7	−3.8	0.53	0.72
FG114	0.39	1.08	2.5	730	−2.6	−3.1	−3.6	0.73	0.87
FG141	0.38	1.15	3.5	850	−1.8	−2.1	−3.2	0.56	0.66
FG142	0.66	1.12	2.9	810	−2.2	−2.5	−3.4	0.64	0.74
FG143	0.63	1.13	2.4	780	−3.1	−3.2	−3.9	0.80	0.82
PLANET	0.28	0.86	4.8	820	−2.9	−3.4	−4.1	0.70	0.83
BOMEX	0.35	1.17	2.5	786	−2.2	−2.5	−2.8	0.77	0.91
Mean	0.42 ±0.15	1.17 ±0.21	3.2 ±0.8		−2.36 ±0.45	−2.77 ±0.42	−3.60 ±0.46	0.66 ±0.11	0.77 ±0.10

of ML slope (Γ_C for the cloud layer and Γ_{CI} for the cloud and inversion layers) show a clear trend—increasing stability (from -2 to -3 K/100 mb) with increasing CBL depth. This seems connected with the more stable double mixing-line structures we saw for the deeper CBLs. For comparison, the slope of the moist adiabat $(\partial\theta_V/\partial p)\theta_{ES} \approx -5.8$ K/100 mb.

The PLANET average is somewhat different from the others with smaller values of β_{SC} and β_C (meaning the cloud layer was relatively better mixed) and larger β_I (a sharper inversion).

c. *Parameterization of mixing-line slope*

The value of Γ^+ is computed from cloud base to a level 70 mb above the CBL top to represent the resolution of CBL top parameters that might be achieved in a typical global forecast model with vertical grid spacing on the order of 70 mb. Table 3 shows the ratios of the slopes

$$R_C = \Gamma_C/\Gamma^+; \quad R_{CI} = \Gamma_{CI}/\Gamma^+.$$

These ratios are considerably less than unity because of the kinks on the θ_V–p^* diagrams (Figs. 29 and 30) above the CBL top, which are associated with the q and θ_E reversals in a layer on the order of 50 mb thick. The vertical solution in a global model is typically inadequate to resolve vertical structure in a 50 mb layer. If we regard the Γ^+ values as global model estimates of the mixing-line slope, we can see that these are significant overestimates of the mixing-line slope within the CBL. Betts and Miller (1985) found that the introduction of an empirical stability parameter (Γ_{CI}/Γ^+ where Γ^+ was computed from one model level above the CBL top) improved the climate of the European Centre forecast model. It is clear that the kinks we see on the conserved variable diagrams above the CBL need more extensive study using other datasets, because their structure is important to boundary layer parameterization in global models.

6. Conclusions

We have found conserved variable methods to be very useful in the study of the thermodynamic structure of the convective boundary layer. Characteristic mixing lines can be seen on θ_E–q or θ_V–p^* diagrams. In the subcloud layer the thermodynamic distribution follows a dry virtual adiabat (constant θ_V). For shallow CBLs (tops $\geq$ 800 mb), a single mixing line is seen through the cloud and inversion layers with a slope about halfway between the dry and moist virtual adiabats. However, the deeper CBLs (top $\leq$ 780 mb) all show a double mixing line with a transition just below the θ_{ES} minimum (the base of the inversion). Some soundings even show a marked q and θ_E reversal between two nearly parallel mixing lines (Fig. 25). We suggest that the precipitation–evaporation processes are responsible for this double ML structure once the CBL (and the deepest clouds in it) reach a sufficient depth. We speculate that perhaps a q and θ_E reversal within the CBL could be maintained by penetrative downdrafts driven by the evaporation of precipitation.

All of the average soundings (except that from BOMEX) show a θ_E and $\mathcal{P}$ minimum, θ_{ES} maximum and local q minimum at the CBL top. The CBL top thus appears on a θ_E–q diagram as a marked kink. This kink marks the top of the layer that is thermodynamically coupled to the surface.

The θ_E and $\mathcal{P}$ minima can be explained in terms of radiative cooling in the air subsiding above the CBL. We estimate that the air has taken about six days to sink from just above the freezing level in a convective disturbance. However, we cannot explain why there is a local reversal of the q gradient in the 50 mb layer above the CBL, although this appears to have been observed frequently. The only process we are aware of that can reverse the normal q gradient is, again, penetrative downdrafts driven by evaporation of falling precipitation. This thermodynamic structure *just above* the CBL, which controls the mixing line slope *within* the CBL, needs further study.

The prediction of the thermodynamic distribution within the CBL (which influences the surface heat and moisture fluxes) is of crucial importance to predicting climate in global models, yet, at present, these models do not have the vertical resolution to resolve the structure we observe just above the CBL.

In general, however, this observational study gives encouragement to the further development of mixing-line models for the parameterization of the CBL. In particular, the specification of the thermodynamic structure of the CBL in terms of the distribution of saturation level $p^*(p)$ along a mixing line (Betts, 1985, 1986) is well supported by this analysis. We suggest $\beta_{SC} = dp^*/dp = 0.3$ for the subcloud layer (along a dry virtual adiabat) and $\beta_C = 1.2$ for the cloud layer.

In future work, we intend to examine the CBL structure for other regions of the Pacific using the FGGE data, compare these results with data from other field experiments, and examine in more detail the balance of convection, radiation and subsidence in maintaining the equilibrium structure of the convective boundary layer over the oceans.

Acknowledgments. This research was supported by National Science Foundation grants ATM 84-03333 and ATM 83-10434 and by National Aeronautics and Space Administration Contract NAS5-28800.

REFERENCES

Albrecht, B. A., V. Ramanathan and B. A. Boville, 1986: The effects of cumulus moisture transports on the simulation of climate with a general circulation model. *J. Atmos. Sci.*, **43**, 2443–2462.

Augstein, E., 1978: The atmospheric boundary layer over the tropical oceans. *Meteorology over the Tropical Oceans.* D. B. Shaw, Ed., Roy. Meteor. Soc., 73–104.

——, and H. Hinzpeter, 1982: The structure of the atmospheric boundary layer under different convection conditions. GATE Monograph, WMO GARP Publ. No. 25, 359–388.

——, H. Riehl, F. Ostapoff and V. Wagner, 1973: Mass and energy transports in an undisturbed Atlantic trade wind flow. *Mon. Wea. Rev.*, **101,** 101–111.

——, H. Schmidt and F. Ostapoff, 1974: The vertical structure of the atmospheric planetary boundary layer in undisturbed trade winds over the Atlantic Ocean. *Bound.-Layer Meteor.*, **6,** 129–150.

Betts, A. K., 1973: Non-precipitating cumulus convection and its parameterization. *Quart. J. Roy. Meteor. Soc.*, **99,** 178–196.

——, 1975: Parametric interpretation of trade-wind cumulus budget studies. *J. Atmos. Sci.*, **32,** 1934–1945.

——, 1976: The thermodynamic transformation of the tropical subcloud layer by precipitation and downdrafts. *J. Atmos. Sci.*, **33,** 1008–1020.

——, 1982: Saturation point analysis of moist convective overturning. *J. Atmos. Sci.*, **39,** 1484–1505.

——, 1983: Thermodynamics of mixed stratocumulus layers: Saturation point budgets. *J. Atmos. Sci.*, **40,** 2655–2670.

——, 1984: Boundary layer thermodynamics of a high plains severe storm. *Mon. Wea. Rev.*, **112,** 2199–2211.

——, 1985: Mixing line analysis of clouds and cloudy boundary layers. *J. Atmos. Sci.*, **42,** 2751–2763.

——, 1986: A new convective adjustment scheme. Part I: Observational and theoretical basis. *Quart. J. Roy. Meteor. Soc.*, **112,** 677–691.

——, and M. J. Miller, 1985: A new convective adjustment scheme for global models. *Seventh Conf. on Numerical Weather Prediction,* Montreal, Amer. Meteor. Soc., 377–383.

——, and ——, 1986: A new convective adjustment scheme. Part II: Single column tests using GATE-Wave, BOMEX, ATEX, and Arctic airmass datasets. *Quart. J. Roy. Meteor. Soc.*, **112,** 693–709.

Byers, H. R., and R. K. Hall, 1955: A census of cumulus cloud height versus precipitation in the vicinity of Puerto Rico during the winter and spring of 1953–54. *J. Meteor.*, **12,** 176–178.

Carlson, T. N., and J. M. Prospero, 1972: The large-scale movement of Saharan air outbreaks over the northern equatorial Atlantic. *J. Appl. Meteor.*, **11,** 283–297.

Deardorff, J. M., 1980: Cloud-top entrainment instability. *J. Atmos. Sci.*, **37,** 131–147.

Ficker, H. von, 1936: Die Passatinversion. *Veroff. Meteor. Inst. Berlin,* **1,** 33 pp.

Firestone, J. K., and B. A. Albrecht, 1986: The structure of the atmospheric boundary layer in the central equatorial Pacific during January and February of FGGE. *Mon. Wea. Rev.*, **114,** 2219–2231.

Holland, J. Z., and E. Rasmusson, 1973: Measurements of the atmospheric mass energy and momentum budgets over a 500 kilometer square of tropical ocean. *Mon. Wea. Rev.*, **101,** 44–55.

Houze, R. A., and A. K. Betts, 1981: Convection in GATE. *Rev. Geophys. Space Phys.*, **19,** 541–576.

Julian, P. R., 1982: The aircraft dropwindsonde system in the Global Weather Experiment. *Bull. Amer. Meteor. Soc.*, **63,** 619–627.

Ludlam, F. H., 1980: *Clouds and Storms.* Pennsylvania State University Press, 405 pp.

Neiburger, M., D. S. Johnson and C. W. Chien, 1961: Studies of the structure of the atmosphere over the eastern Pacific Ocean in summer. Pt. I. The inversion over the eastern North Pacific. *Univ. Calif. Publ. Meteor.*, **1,** 1–94.

Nicholls, S., 1984: The dynamics of stratocumulus: Aircraft observations and comparisons with a mixed layer model. *Quart. J. Roy. Meteor. Soc.*, **110,** 783–820.

Nitta, T., and S. Esbensen, 1974: Heat and moisture budgets using BOMEX data. *Mon. Wea. Rev.*, **102,** 17–28.

Paluch, I. R., 1979: The entrainment mechanism in Colorado cumuli. *J. Atmos. Sci.*, **36,** 2467–2478.

Riehl, H., 1954: *Tropical Meteorology.* McGraw-Hill, 392 pp.

——, 1979: *Climate and Weather in the Tropics.* Academic Press, 611 pp.

——, T. C. Yeh, J. S. Malkus and N. E. LaSeur, 1951: The northeast trade of the Pacific Ocean. *Quart. J. Roy. Meteor. Soc.*, **77,** 598–626.

Rossby, C. G., 1932: Thermodynamics applied to air mass analysis. *Meteor. Pap.*, Vol. I, Massachusetts Institute of Technology, 7–24.

Zipser, E. J., 1969: The role of organized, unsaturated convective downdrafts in the structure and rapid decay of an equatorial disturbance. *J. Appl. Meteor.*, **8,** 799–814.